energies

MDPI

Article

High-Order AVO Inversion for Effective Pore-Fluid Bulk Modulus Based on Series Reversion and Bayesian Theory

Lei Shi [1], Yuhang Sun [2,*], Yang Liu [2,3], David Cova [2] and Junzhou Liu [1]

[1] SINOPEC Exploration Production Research Institute, Haidian District, Beijing 100083, China; shilei2009.syky@sinopec.com (L.S.); liujz.syky@sinopec.com (J.L.)
[2] College of Geophysics, China University of Petroleum—Beijing, Changping District, Beijing 102249, China; liuyang@cup.edu.cn (Y.L.); dcovat@gmail.com (D.C.)
[3] College of Petroleum, China University of Petroleum—Beijing at Karamay, Karamay, Xinjiang 834000, China
* Correspondence: 2018315022@student.cup.edu.cn; Tel.: +86-1501-007-0100

Received: 31 January 2020; Accepted: 6 March 2020; Published: 12 March 2020

Abstract: Pore-fluid identification is one of the key technologies in seismic exploration. Fluid indicators play important roles in pore-fluid identification. For sandstone reservoirs, the effective pore-fluid bulk modulus is more susceptible to pore-fluid than other fluid indicators. AVO (amplitude variation with offset) inversion is an effective way to obtain fluid indicators from seismic data directly. Nevertheless, current methods lack a high-order AVO equation for a direct, effective pore-fluid bulk modulus inversion. Therefore, based on the Zoeppritz equations and Biot–Gassmann theory, we derived a high-order P-wave AVO approximation for an effective pore-fluid bulk modulus. Series reversion and Bayesian theory were introduced to establish a direct non-linear P-wave AVO inversion method. By adopting this method, the effective pore-fluid bulk modulus, porosity, and density can be inverted directly from seismic data. Numerical simulation results demonstrate the precision of our proposed method. Model and field data evaluations show that our method is stable and feasible.

Keywords: the effective pore-fluid bulk modulus; high order AVO equation; series reversion; Bayesian theory

1. Introduction

Pore-fluid identification remains a key part of hydrocarbon reservoir exploration. Fluid indicators are crucial to distinguishing pore-fluid. The first fluid indicator is defined as the weighting difference of P- and S-wave velocities (Smith and Gidlow, 1987) [1]. Hence, Fatti et al. (1994) proposed the weighting difference of P- and S-wave reflection coefficients as a fluid indicator [2]. As the recognition technology developed, the definition of the fluid indicator expanded into the impedance domain. Goodway et al. (1997) showed the advantages of Lamé parameters in fluid discrimination while lithologic parameters remained unchanged [3]; however, the identification accuracy of Lamé parameters will decrease if lithologic parameters change. Quakenbush et al. (2006) defined a fluid indicator with a bulk modulus, which was more sensitive to pore-fluid and more independent of a rock matrix than the Lamé parameters [4]. Russell et al. (2011) generalized the fluid indicator to a Gassmann fluid factor and enhanced the ability to distinguish pore-fluid [5]. Most conventional fluid indicators are a combination of density and velocity. However, these fluid indicators can often provide uncertain results when determining fluids because their sensitivity is conditional on the mixed effects of pore-fluid and rock matrices (Zhang et al., 2010) [6]. To improve the accuracy of fluid identification, Yin and Zhang (2014) presented an effective pore-fluid bulk modulus as a fluid indicator. It has been proven that the

effective pore-fluid bulk modulus is advantageous in identifying reservoirs because it is only related to pore-fluid [7].

AVO inversion is a useful tool to extract fluid indicators from seismic data directly. AVO inversion methods can be divided into linear and nonlinear methods. The former uses linear AVO approximations to establish inversion equations, while the latter uses exact expressions or high order AVO approximations. Yin and Zhang (2014) deduced a linear four-term AVO approximation and proposed a Bayesian AVO inversion method for an effective pore-fluid bulk modulus. By using this method, the effective pore-fluid bulk modulus could be inverted from seismic data directly [7]. However, the four terms of this approximation are not completely independent, and this method needs four angle gathers. Yin et al. (2018) put forward a new linear three-term AVO approximation and enhanced the stability of inversion [8]. Nevertheless, we must analyze the exponential relationship between porosity and shear modulus when we invert field data by employing this approximation. Linear approximations have high precision under small incident angles and parameter differences at both sides of an interface; however, they will suffer a loss of accuracy with increasing incident angles and parameter differences. At present, neither exact nor nonlinear equations exist for an effective pore-fluid bulk modulus.

In this paper, an effective pore-fluid bulk modulus is considered as a fluid indicator. Based on Zoeppritz equations and the Biot–Gassmann theory, we first deduce a high-order AVO approximation for the effective pore-fluid bulk modulus. Consequently, a direct nonlinear AVO inversion method is formulated for the fluid indicator in a series reversion and Bayesian theory framework. Model and field data tests follow.

2. Theory and Method

2.1. Sensitivity Analysis of the Effective Pore-Fluid Bulk Modulus

Various fluid indicators have been proposed to identify pore-fluid. In this section, we analyze the sensitivity of several commonly used fluid indicators to detect pore-fluid changes in sandstone reservoirs. By using the three types of sandstone model displayed in Table 1 [9], the P-wave modulus, Gassmann fluid factor, and effective pore-fluid bulk modulus are computed. The calculation results are shown in Table 2. To analyze the sensitivity of these three fluid indicators, we define the relative variation as an identified parameter and visualize this identified parameter in the bar graph (Figure 1). The larger the relative variation value is, the more sensitive the fluid indicator is to the change of pore-fluid. The relative variations of the effective pore-fluid bulk modulus are the largest in all of the three pictures in Figure 1. This demonstrates that the effective pore-fluid bulk modulus has more advantages in identifying pore-fluid than the other two fluid indicators did.

Table 1. Three types of sandstone models by Hilterman (2001) [9].

Type	Pore-Fluid	P-Wave Velocity (m/s)	S-Wave Velocity (m/s)	Density (g/cm^3)	Porosity (%)
1	Water	4115	2453	2.32	15
	Gas	4050	2526	2.21	20
2	Water	3048	1595	2.23	15
	Gas	2781	1665	2.08	20
3	Water	2134	860	2.11	15
	Gas	1543	901	1.88	20

Table 2. The calculation results of fluid indicators in sandstone models.

Type	Pore-Fluid	P-wave Modulus (GPa)	Gassmann Fluid Factor (GPa)	Effective Pore-Fluid Bulk Modulus (GPa)
1	Water	39.29	−16.56	−17.66
	Gas	36.25	−20.16	−12.90
2	Water	20.72	−19.75	−21.07
	Gas	16.09	−6.98	−5.58
3	Water	9.61	3.37	3.59
	Gas	4.48	−1.63	−1.70

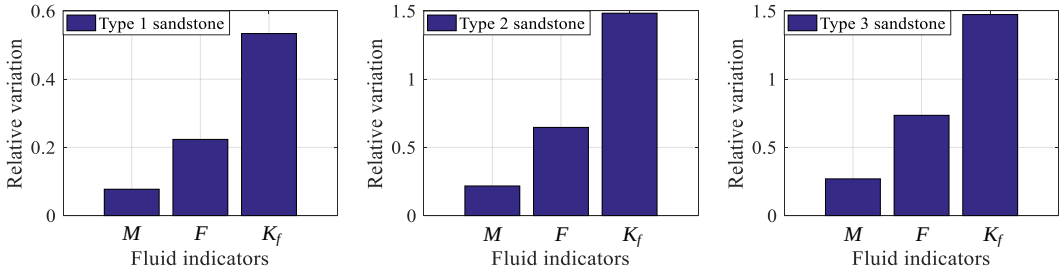

(**a**) (**b**) (**c**)

Figure 1. The relative variations of fluid indicators in sandstone models: (**a**) Type 1; (**b**) Type 2; (**c**) Type 3. M, F, and K_f represent the P-wave modulus, Gassmann fluid factor, and the effective pore-fluid bulk modulus.

2.2. P-Wave High-Order AVO Approximations for the Effective Pore-Fluid Bulk Modulus

An effective pore-fluid bulk modulus has shown a clear advantage as a fluid indicator for identifying pore-fluid. AVO inversion is a useful technology for extracting an effective pore-fluid bulk modulus from seismic data directly, though a high-order approximation for inversion is nonexistent. Here, a new estimation is deduced based on the Zoeppritz equations and Biot–Gassmann theory. The Zoeppritz equations are the foundation of AVO methodology [10]. Based on the relationships among seismic amplitudes, this equation can be expressed as (Keys, 1989) [11]

$$\begin{bmatrix} -X & -\sqrt{1-B^2X^2} & CX & -\sqrt{1-D^2X^2} \\ \sqrt{1-X^2} & -BX & \sqrt{1-C^2X^2} & DX \\ 2B^2X\sqrt{1-X^2} & B\left(1-2B^2X^2\right) & 2AD^2X\sqrt{1-C^2X^2} & -AD\left(1-2D^2X^2\right) \\ -\left(1-2B^2X^2\right) & 2B^2X\sqrt{1-B^2X^2} & AC\left(1-2D^2X^2\right) & 2AD^2X\sqrt{1-D^2X^2} \end{bmatrix} \begin{bmatrix} R_{PP} \\ R_{PS} \\ T_{PP} \\ T_{PS} \end{bmatrix} = \begin{bmatrix} X \\ \sqrt{1-X^2} \\ 2B^2X\sqrt{1-X^2} \\ 1-2B^2X^2 \end{bmatrix}, \quad (1)$$

where X represents $\sin\theta$, with θ as the incident angle; R_{PP} and R_{PS} are P- and S-wave reflection coefficients, respectively; and T_{PP} and T_{PS} are P- and S-wave transmission coefficients, respectively.

For the incident P-wave case, A, B, C, and D are defined as (Kim and Innanen, 2013) [12]

$$A = \left(1 - \frac{\Delta\rho}{\overline{\rho}}\right)^{-1}, \quad (2a)$$

$$B = \gamma_{sat}^{-1}, \quad (2b)$$

$$C = \left\{\left(1 - \frac{\Delta\rho}{\overline{\rho}}\right)\left[\frac{\gamma_{dry}^2}{\gamma_{sat}^2}\left(1 - \frac{\Delta\mu}{\overline{\mu}}\right)^{-1} + \left(1 - \frac{\gamma_{dry}^2}{\gamma_{sat}^2}\right)\left(1 - \frac{\Delta f}{\overline{f}}\right)^{-1}\right]\right\}^{\frac{1}{2}}, \quad (2c)$$

$$D = \left[\gamma_{sat}^{-2}\left(1 - \frac{\Delta\mu}{\overline{\mu}}\right)^{-1}\left(1 - \frac{\Delta f}{\overline{f}}\right)\right]^{\frac{1}{2}}, \quad (2d)$$

where γ_{dry} and γ_{sat} denote the velocity ratios of P- and S-wave in dry rock and saturated rock, respectively. $\Delta f/\overline{f}$, $\Delta\mu/\overline{\mu}$ and $\Delta\rho/\overline{\rho}$ are calculated by

$$\frac{\Delta f}{\overline{f}} = \frac{2(f_{i+1} - f_i)}{(f_{i+1} + f_i)}, \tag{3a}$$

$$\frac{\Delta \mu}{\overline{\mu}} = \frac{2(\mu_{i+1} - \mu_i)}{(\mu_{i+1} + \mu_i)}, \tag{3b}$$

$$\frac{\Delta \rho}{\overline{\rho}} = \frac{2(\rho_{i+1} - \rho_i)}{(\rho_{i+1} + \rho_i)}, \tag{3c}$$

where f and μ represent the Gassmann fluid factor and shear modulus, respectively, which can be calculated by (Russell et al., 2011) [5]

$$f = \rho\alpha^2 - \gamma_d^2\mu, \tag{4a}$$

$$\mu = \rho\beta^2, \tag{4b}$$

where ρ is density, and i and $i+1$ are the upper and lower layers of the interface, respectively.

According to the Gassmann equation, the Gassmann fluid factor can be derived as (Han and Batzle, 2003) [13]

$$f = GK_f, \tag{5}$$

where K_f is the effective pore-fluid bulk modulus, and

$$G = \frac{(1 - K_n)^2}{\phi}, \tag{6a}$$

$$K_n = \frac{K_{dry}}{K_s}, \tag{6b}$$

where ϕ, K_s, and K_{dry} stand for the porosity of porous rock, the bulk modulus of solid grain, and the bulk modulus of dry porous rock, respectively.

Based on the critical porosity model, Nur et al. (1998) provide the following equations [14]:

$$K_{dry} = K_s\left(1 - \frac{\phi}{\phi_c}\right), \tag{7a}$$

$$\mu_{dry} = \mu_s\left(1 - \frac{\phi}{\phi_c}\right), \tag{7b}$$

where ϕ_c, μ_s, and μ_{dry} denote critical porosity, the shear modulus of solid grain, and the shear modulus of dry porous rock, respectively.

For the same reservoir, we assume that critical porosity is constant. Replacing μ with μ_{dry}, and substituting Equations (5) and (7a,b) into Equation (2a–d), we have

$$A = \left(1 - \frac{\Delta\rho}{\overline{\rho}}\right)^{-1}, \tag{8a}$$

$$B = \gamma_{sat}^{-1}, \tag{8b}$$

$$C = \left\{\left(1 - \frac{\Delta\rho}{\overline{\rho}}\right)\left[\left(\frac{\gamma_{dry}^2}{\gamma_{sat}^2}\right)\left(1 - \gamma_\phi\frac{\Delta\phi}{\overline{\phi}}\right)^{-1} + \left(1 - \frac{\gamma_{dry}^2}{\gamma_{sat}^2}\right)\left(1 - \frac{\Delta\phi}{\overline{\phi}} - \frac{\Delta K_f}{\overline{K}_f}\right)^{-1}\right]\right\}^{\frac{1}{2}}, \tag{8c}$$

$$D = \left[\gamma_{sat}^{-2}\left(1 - \gamma_\phi \frac{\Delta\phi}{\overline{\phi}}\right)^{-1}\left(1 - \frac{\Delta\rho}{\overline{\rho}}\right)\right]^{\frac{1}{2}}. \tag{8d}$$

By substituting Equation (8a–d) into (1) and applying the Taylor expansion to $\Delta K_f/\overline{K}_f$, $\Delta\phi/\overline{\phi}$ and $\Delta\rho/\overline{\rho}$, the P-wave reflection coefficient is deduced as follows:

$$R_{pp} = R_{pp}^{(1)} + R_{pp}^{(2)} + R_{pp}^{(3)} + \ldots, \tag{9}$$

where, $R_{pp}^{(i)}$ $(i = 1, 2, 3, \ldots)$ are the different order terms of P-wave reflection coefficients, involving the effective pore-fluid bulk modulus, porosity, and density. The *i*th-order approximation is written as $R_{pp} = R_{pp}^{(1)} + \ldots + R_{pp}^{(i)}$ $(i = 1, 2, 3, \ldots)$. Using the method of numerical analysis, we study the effect of the expansion order number on the accuracy of the deduced approximation. For small incident angle and parameter differences across the interface, the relative errors of different order approximations are all less than 1%. With an increase of the incident angle and parameter differences across the interface, the accuracy of the first- and second-order approximations decreases heavily. The relative error of the third-order approximation increases but is still less than 1%. When the expansion order number is greater than 3, the accuracy of the deduced approximation increases slightly, but the calculation efficiency decreases heavily. We considered both accuracy and efficiency, and decided to use the third-order approximation, which is expressed as

$$R_{pp} = R_{pp}^{(1)} + R_{pp}^{(2)} + R_{pp}^{(3)}, \tag{10a}$$

$$R_{pp}^{(1)} = W_{11}\frac{\Delta K_f}{\overline{K}_f} + W_{12}\frac{\Delta\phi}{\overline{\phi}} + W_{13}\Delta\frac{\Delta\rho}{\overline{\rho}}, \tag{10b}$$

$$R_{pp}^{(2)} = W_{21}\left(\frac{\Delta K_f}{\overline{K}_f}\right)^2 + W_{22}\left(\frac{\Delta\phi}{\overline{\phi}}\right)^2 + W_{23}\left(\frac{\Delta\rho}{\overline{\rho}}\right)^2 + W_{24}\left(\frac{\Delta K_f}{\overline{K}_f}\right)\left(\frac{\Delta\phi}{\overline{\phi}}\right) + W_{25}\left(\frac{\Delta K_f}{\overline{K}_f}\right)\left(\frac{\Delta\rho}{\overline{\rho}}\right) + W_{26}\left(\frac{\Delta\phi}{\overline{\phi}}\right)\left(\frac{\Delta\rho}{\overline{\rho}}\right), \tag{10c}$$

$$\begin{aligned} R_{pp}^{(3)} = {} & W_{30}\left(\frac{\Delta K_f}{\overline{K}_f}\right)^3 + W_{31}\left(\frac{\Delta\phi}{\overline{\phi}}\right)^3 + W_{32}\left(\frac{\Delta\rho}{\overline{\rho}}\right)^3 + W_{33}\left(\frac{\Delta K_f}{\overline{K}_f}\right)^2\left(\frac{\Delta\phi}{\overline{\phi}}\right) + W_{34}\left(\frac{\Delta K_f}{\overline{K}_f}\right)^2\left(\frac{\Delta\rho}{\overline{\rho}}\right) + W_{35}\left(\frac{\Delta\phi}{\overline{\phi}}\right)^2\left(\frac{\Delta K_f}{\overline{K}_f}\right) \\ & + W_{36}\left(\frac{\Delta\phi}{\overline{\phi}}\right)^2\left(\frac{\Delta\rho}{\overline{\rho}}\right) + W_{37}\left(\frac{\Delta\rho}{\overline{\rho}}\right)^2\left(\frac{\Delta K_f}{\overline{K}_f}\right) + W_{38}\left(\frac{\Delta\rho}{\overline{\rho}}\right)^2\left(\frac{\Delta\phi}{\overline{\phi}}\right) + W_{39}\left(\frac{\Delta K_f}{\overline{K}_f}\right)\left(\frac{\Delta\phi}{\overline{\phi}}\right)\left(\frac{\Delta\rho}{\overline{\rho}}\right). \end{aligned} \tag{10d}$$

Using the sand model in Table 3 (Yin and Zhang, 2014) [7], we compare the accuracy of these approximations. P-wave reflection coefficients are computed through the Zoeppritz equations [10], Aki–Richards approximation (Aki and Richards, 1980) [15], and different order approximations, respectively. As shown in Figure 2a, the curves of the Aki–Richards approximation and different order approximations all are close to the Zoeppritz curve. Small elastic parameter perturbations across reflectors are caused only by pore-fluid (Model 1). In Figure 2b,c, note that the AVO curves computed from the Aki–Richards approximation and different order approximations are close to the Zoeppritz curve for incident angles less than 30°. However, for larger incident angles the curve of the deduced third-order approximation is the closest to the Zoeppritz curve. This is because the elastic parameter perturbations across reflectors are caused by only porosity or both pore-fluid and porosity (Models 2 and 3).

Table 3. Parameters of the sand model (Yin and Zhang, 2014) [7].

	Pore-Fluid	K_f (GPa)	ρ (g/cm^3)	V_p (m/s)	V_s (m/s)	ϕ (%)	ϕ_c (%)
Model 1	Gas	0.10	1.99	1920	1230	25	40
	Water	2.38	2.26	2590	1150	25	40
Model 2	Water	2.38	2.26	2590	1150	25	40
	Water	2.38	2.34	3580	2070	25	40
Model 3	Gas	0.10	2.12	3340	2170	25	40
	Water	2.38	2.26	2590	1150	25	40

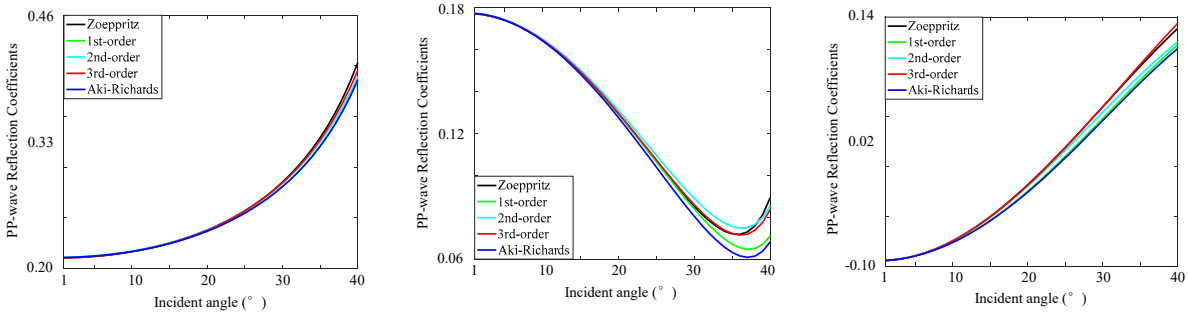

Figure 2. P-wave reflection coefficients computed by different equations: (**a**) Model 1; (**b**) Model 2; (**c**) Model 3.

Next, we analyze the information contained in reflections and the stability of inversion for the first-order approximation. If the second- and higher-order terms of Equation (9) are neglected, it becomes a linear approximation. The P-wave reflection coefficient is written as

$$R_{pp} \approx R_{pp}^{(1)} = \left[\left(\frac{1}{4} - \frac{1}{4}\frac{\gamma_{dry}^2}{\gamma_{sat}^2}\right)\sec^2\theta\right]\frac{\Delta K_f}{\overline{K}_f} + \left[-2\frac{1}{\gamma_{sat}^2}\gamma_\phi \sin^2\theta + \left(\frac{1}{4} - \frac{1}{4}\frac{\gamma_{dry}^2}{\gamma_{sat}^2} + \frac{1}{4}\frac{\gamma_{dry}^2}{\gamma_{sat}^2}\gamma_\phi\right)\sec^2\theta\right]\frac{\Delta\phi}{\overline{\phi}} + \left(-\frac{1}{4}\sec^2\theta + \frac{1}{2}\right)\frac{\Delta\rho}{\overline{\rho}}. \quad (11)$$

In this equation, the effective pore-fluid bulk modulus, porosity, and density have different proportions of information in their reflection coefficients. As a result, the stability of inversion for these three elastic parameters is different. Equation (11) can be expressed as

$$R_{pp} = \begin{bmatrix} \left(\frac{1}{4} - \frac{1}{4}\frac{\gamma_{dry}^2}{\gamma_{sat}^2}\right)\sec^2\theta \\ \left[-2\frac{1}{\gamma_{sat}^2}\gamma_\phi \sin^2\theta + \left(\frac{1}{4} - \frac{1}{4}\frac{\gamma_{dry}^2}{\gamma_{sat}^2} + \frac{1}{4}\frac{\gamma_{dry}^2}{\gamma_{sat}^2}\gamma_\phi\right)\sec^2\theta\right] \\ -\frac{1}{4}\sec^2\theta + \frac{1}{2} \end{bmatrix}^{\mathrm{T}} \begin{bmatrix} \frac{\Delta K_f}{\overline{K}_f} \\ \frac{\Delta\phi}{\overline{\phi}} \\ \frac{\Delta\rho}{\overline{\rho}} \end{bmatrix}, \quad (12)$$

where the first term on the right of Equation (12) is the mapping operator between elastic parameters and reflection coefficients.

Nicolao et al. (1993) proposed that the eigenvalues of this mapping operator matrix can be used to measure the information of elastic parameters [16]. The eigenvalues are proportional to the information content. The direction cosine of the eigenvector of the mapping operator matrix can reflect the difficulty of inverting these elastic parameters. The greater the absolute value of the direction cosine is, the easier the inversion is. Moreover, when the direction cosine equals zero, the inversion is unviable. By using the first model in Table 3, the eigenvalues corresponding to the effective pore-fluid bulk modulus, porosity, and density are shown in Figure 3a. When the incident angle is smaller than 30°, the energy

of the first eigenvalue (blue) is larger than that of the second eigenvalue (red) and the third eigenvalue (black). Consequently, we only need to analyze the eigenvector of the first eigenvalue to get a different degree in inverting these elastic parameters. As displayed in Figure 3b, the direction cosine of the effective pore-fluid bulk modulus, porosity, and density is far away from zero. This means that these three elastic parameters can be inverted by Equation (11).

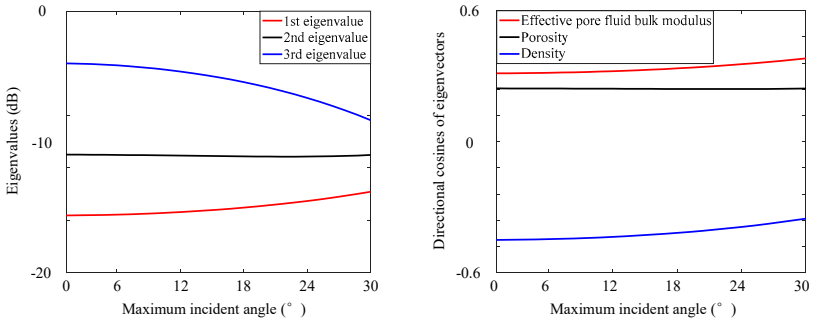

(**a**) (**b**)

Figure 3. (**a**) Comparisons of three eigenvalues vs the maximum incident angle in the data domain; (**b**) Comparisons of directional cosines of the first eigenvector vs the maximum incident angle in the model domain.

The stability of inversion is very important. Therefore, the method proposed by Yin et al. (2018) is used to analyze the stability of Equation (11). Yin et al. (2018) deduced a three-term linear approximation including the effective pore-fluid bulk modulus [8], an approximation of which can be displayed as

$$R_{pp} = \left[\left(\frac{1}{4} - \frac{1}{4}\frac{\gamma_{dry}^2}{\gamma_{sat}^2}\right)\sec^2\theta\right]\frac{\Delta K_f}{\overline{K}_f} + \left[\left(\frac{\gamma_{dry}^2}{4\gamma_{sat}^2} - \frac{2}{\gamma_{sat}^2}\sin^2\theta\right) + \frac{1}{r}\left(\frac{\sec^2\theta}{4} - \frac{\gamma_{dry}^2}{2\gamma_{sat}^2}\sec^2\theta + \frac{2}{\gamma_{sat}^2}\sin^2\theta\right)\right]\frac{\Delta f_m}{\overline{f}_m} + \left(-\frac{1}{4}\sec^2\theta + \frac{1}{2}\right)\frac{\Delta\rho}{\overline{\rho}}, \quad (13)$$

where $f_m = \phi\mu$, r is the fit coefficient of ϕ and μ according to field data.

The logarithm of the condition number of weighting coefficients can measure the stability of the inversion equation. The smaller the logarithm is, the more stable the inversion is. We compute the values of Equations (11) and (13), the results of which are shown in Figure 4. With the increase of incident angle, both of these two conditional numbers decrease. However, the conditional number of Equation (13) is larger than that of Equation (11). This indicates that the stability of inverting the effective pore-fluid bulk modulus, porosity, and density increases with an increase in the incident angle, and that the stability of Equation (11) is better than that of Equation (13).

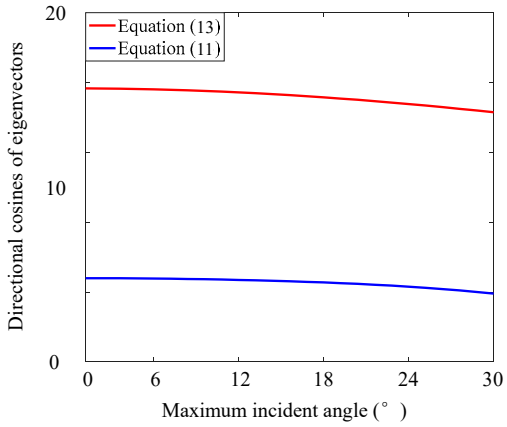

Figure 4. Analysis of the condition number of the coefficient matrix in Equations (11) and (13).

The weighting coefficients before elastic parameters in Equation (11) include $\gamma_{dry}^2/\gamma_{sat}^2$. γ_{sat} is the ratio of P- to S-wave velocities in saturated rock and can be calculated by logging data, while γ_{dry} is the ratio of P- to S-wave velocities in dry rock. Russell et al. (2003, 2006, 2011) [5,17,18] estimated the value of γ_{dry}^2 through theoretical analysis and practical calculations, and proposed a possible range value for γ_{dry}^2.

Here, we analyze the effect of $\gamma_{dry}^2/\gamma_{sat}^2$ on the weighting coefficients of the effective pore-fluid bulk modulus, porosity, and density. According to Russell et al. (2011) [5], we assume that γ_{sat}^2 is 4 and γ_{dry}^2 is 2.33, 2.50, and 3.00, respectively. As shown in Figure 5, the weighting coefficient curves of these three elastic parameters are computed with an incident angle from 0° to 45°. With the variation of γ_{dry}^2, the pore-fluid bulk modulus (Figure 5a) and porosity (Figure 5b) curves change, while the density curve (Figure 5c) is unaffected. Therefore, $\gamma_{dry}^2/\gamma_{sat}^2$ influences only the effective pore-fluid bulk modulus and porosity, while the density is unchanged.

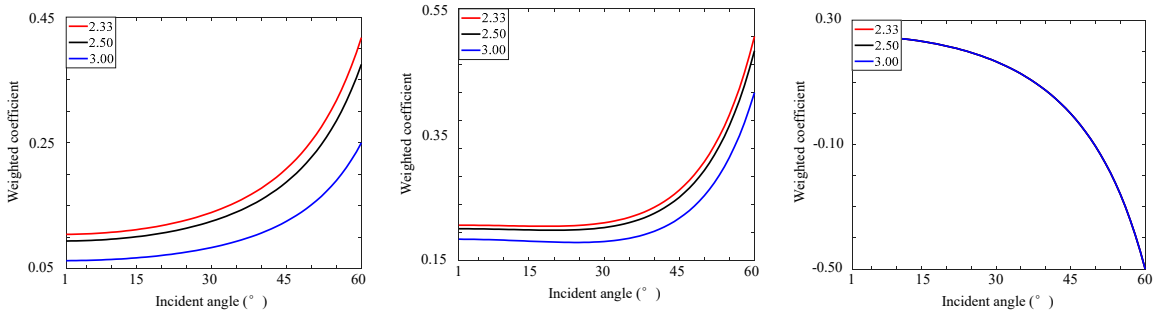

(**a**) (**b**) (**c**)

Figure 5. Weighting coefficients of $\gamma_{dry}^2 = 2.33$, $\gamma_{dry}^2 = 2.50$, and $\gamma_{dry}^2 = 3.00$. (**a**) The effective pore-fluid bulk modulus; (**b**) porosity; (**c**) density.

In this paper, we use the third-order approximation to establish a nonlinear AVO inversion method. This approximation includes the first-, second-, and third-order terms:

$$R_{pp} \approx R_{pp}^{(1)} + R_{pp}^{(2)} + R_{pp}^{(3)}. \tag{14}$$

2.3. Effective Pore-Fluid Bulk Modulus Nonlinear AVO Inversion Method

AVO inversion includes linear and nonlinear approaches. By adopting the third-order approximation, the AVO inversion method is strictly nonlinear. Because the efficiency of the nonlinear inversion method is pretty low in practice, series reversion is applied. Series reversion is an effective

approach to transforming a nonlinear relationship into a linear relationship (Frank and Tat, 2001) [19]. For example, for the expression

$$y = \frac{x}{1-x} = \sum_{i=1}^{n} x^i, \tag{15}$$

the solution is

$$x = y/(1+y). \tag{16}$$

By using series reversion to solve Equation (15), x can be expanded in series as

$$y = \sum_{i=1}^{n} x_i, \tag{17}$$

where x_i is the ith-order item of y.

Substituting Equation (17) into (15), we can express x_i as

$$x_i = (-1)^{i+1} y^i, \qquad i = 1, 2, \ldots, n. \tag{18}$$

By adopting Equation (18) into (17), x can be calculated as

$$x = x_1 + x_2 + x_3 + \ldots = y - y^2 + y^3 + \ldots = y/(1-y). \tag{19}$$

In this way, the P-wave reflection coefficient, the effective pore-fluid bulk modulus, porosity, and density can be expanded in series. There are some tests for the effect of the expansion item number on accuracy and efficiency. When these parameters are expanded into three items, this method has advantages in both accuracy and efficiency. These parameters can be expressed as

$$R_{pp} = R_{pp_1} + R_{pp_2} + R_{pp_3}, \tag{20a}$$

$$K_f = K_{f_1} + K_{f_2} + K_{f_3}, \tag{20b}$$

$$\phi = \phi_1 + \phi_2 + \phi_3\,, \tag{20c}$$

$$\rho = \rho_1 + \rho_2 + \rho_3\,. \tag{20d}$$

Combining Equation (20a–d) with (10a–d), we obtain

$$R_{pp3} = R_{pp}^{(1)}(K_{f3}, \phi_3, \rho_3) + R_{pp}^{(2)}(K_{f2}, \phi_2, \rho_2) + R_{pp}^{(3)}(K_{f2}, \phi_2, \rho_2) + R_{pp}^{(3)}(K_{f1}, \phi_1, \rho_1), \tag{21a}$$

$$R_{pp2} = R_{pp}^{(1)}(K_{f2}, \phi_2, \rho_2) + R_{pp}^{(2)}(K_{f1}, \phi_1, \rho_1), \tag{21b}$$

$$R_{pp1} = R_{pp}^{(1)}(K_{f1}, \phi_1, \rho_1). \tag{21c}$$

Additionally, using the approach of Zhang and Weglein (2009) [20], we can calculate R_{pp1}, R_{pp2}, and R_{pp3} through R_{pp} in four steps. First, according to Equation (21c), K_{f1}, ϕ_1, and ρ_1 are inverted by the Bayesian theory. Second, K_{f2}, ϕ_2, and ρ_2 are inverted via the least square method based on Equation (21b). Third, K_{f3}, ϕ_3, and ρ_3 are inverted using the last step from Equation (21a). Finally, K_f, ϕ, and ρ are computed using Equation (20a–d).

In the first three steps, a linear inversion AVO method is functional. The AVO inversion is based on the convolution model, which is written as

$$\mathbf{d=WR=WGm}, \tag{22}$$

where, **d**, **W**, **m**, and **G** are the seismic data, seismic wavelet, elastic parameters, and mapping operator between **d** and **m**, respectively. Because **G** is usually an irreversible matrix, its conjugate matrix is

commonly adopted to solve Equation (22). In general, the objective function of AVO inversion takes the form of an L2 norm, which is expressed as

$$J_{\min} = \frac{1}{2}\int (\mathbf{Gm} - \mathbf{d})^2 dt. \tag{23}$$

AVO inversion is an ill-conditioned and ill-posed problem. The single point estimation method is commonly used to obtain optimal solutions for the objective function. However, it is unable to evaluate solutions. Thus, this paper introduces the Bayesian inversion theory. The mathematical expression of the Bayesian theory can be expressed as

$$P(\mathbf{m}|\mathbf{d}) = P(\mathbf{d}|\mathbf{m})P(\mathbf{m})/P(\mathbf{d}), \tag{24}$$

where $P(\mathbf{m}|\mathbf{d})$ denotes the posterior probability function, $P(\mathbf{d}|\mathbf{m})$ is the likelihood function, $P(\mathbf{m})$ represents the prior distribution function (on which the results of this theory mainly depend), and $P(\mathbf{d})$ is marginal distribution, which is always a constant. It is assumed that the prior information complies with multivariate Cauchy distribution, which is expressed as

$$P(\mathbf{m}) = P_{om} \exp\left[-2\sum_{i=1}^{N} \ln\left(1 + \mathbf{m}^T \mathbf{\Phi}^i \mathbf{m}\right)\right], \tag{25a}$$

$$P_{om} = \frac{1}{\pi^{2N} |\mathbf{\Psi}|^{N/2}}, \tag{25b}$$

$$\mathbf{\Phi} = \left(\mathbf{D}^i\right)^T \mathbf{\Psi}^{-1} \mathbf{D}^i, \tag{25c}$$

$$D^i_{nl} = \begin{cases} 1, & n = 1, l = i \\ 1, & n = 2, l = i + N \\ 1, & n = 3, l = i + 2N \\ 0, & else \end{cases}, \tag{25d}$$

where N is the number of samples, and $\mathbf{\Psi}$ is a 3×3 scale matrix.

The likelihood function obeys multivariate Gaussian distribution as

$$P(\mathbf{d}|\mathbf{m}) = \frac{1}{(2\pi)^{\frac{N}{2}} \sqrt{\det \mathbf{C_d}}} \exp\left\{-\frac{1}{2}(\mathbf{d} - \mathbf{Gm})^T \mathbf{C_d}^{-1} (\mathbf{d} - \mathbf{Gm})\}\right\}, \tag{26}$$

where $\mathbf{C_d}$ denotes the noise covariance matrix.

The posterior probability distribution of parameters to be solved can be indicated as

$$P(\mathbf{m}|\mathbf{d}) = \left\{-\frac{1}{2}(\mathbf{d\text{-}Gm})^T \mathbf{C_d}^{-1} (\mathbf{d\text{-}Gm}) - 2\sum_{i=1}^{N} \ln\left(1 + \mathbf{m}^T \mathbf{\Phi}^i \mathbf{m}\right)\right\}. \tag{27}$$

In terms of Equations (23) and (27), the objective function becomes

$$J(\mathbf{m}) = \frac{1}{2}(\mathbf{d\text{-}Gm})^T \mathbf{C_d}^{-1} (\mathbf{d\text{-}Gm}) + 2\sum_{i=1}^{N} \ln\left(1 + \mathbf{m}^T \mathbf{\Phi}^i \mathbf{m}\right). \tag{28}$$

By taking the derivative of Equation (28) with respect to $\mathbf{m}$, $\mathbf{m}$ is given.

3. Results

In this section, a logging model and field data are used to validate the advantages of our new inversion method.

3.1. Model Data Test

A logging model from sandstone reservoirs was used to verify the feasibility of our inversion method. The synthetic seismic record generated by the Ricker wavelet with a dominant frequency of 25 Hz is shown in Figure 6a (without noise) and Figure 6b (signal-to-noise ratio equals 2). Figure 7a displays the inverted results of the synthetic gather without noise. The logging data, elastic parameters inverted by the previous linear method (Yin et al., 2018), and proposed nonlinear method in this paper are shown using black, green, and red lines. The errors between the logging data and the inverted results are displayed in Figure 7b. The inversion results of the effective pore-fluid bulk modulus, porosity, and density had the same trend as the logging data, while the curves of the proposed nonlinear method were closer to the logging data curves. Figure 7c displays the values of L2 norm and shows that these two methods could obtain a satisfactory result within five iterations. The final value of the L2 norm in the proposed method case was smaller than that in the method of Yin et al. (2018). Furthermore, we added noise to the synthetic angle gathers, as shown in Figure 6b. The inverted elastic parameters of the synthetic angle gathers with and without noise are displayed in Figure 8a. Figure 8b shows the errors of logging data and the inverted results. The error difference was relatively larger in the noise case than in the noise-free case. However, the error between inverted elastic parameters and logging data was not so severe. As can be seen in Figure 8c, the curves of the L2 norm were close. Using the synthetic gathers without noise, we compared the accuracy and efficiency of the proposed nonlinear method and the traditional fully nonlinear method (Zhou et al., 2016) [21]. Figure 9a shows the inverted results of these two methods. The inverted values were both close to those of the logging data. The curves of error are displayed in Figure 9b, without much difference between the curves. However, the traditional fully nonlinear method took about 15 times as long as the proposed method.

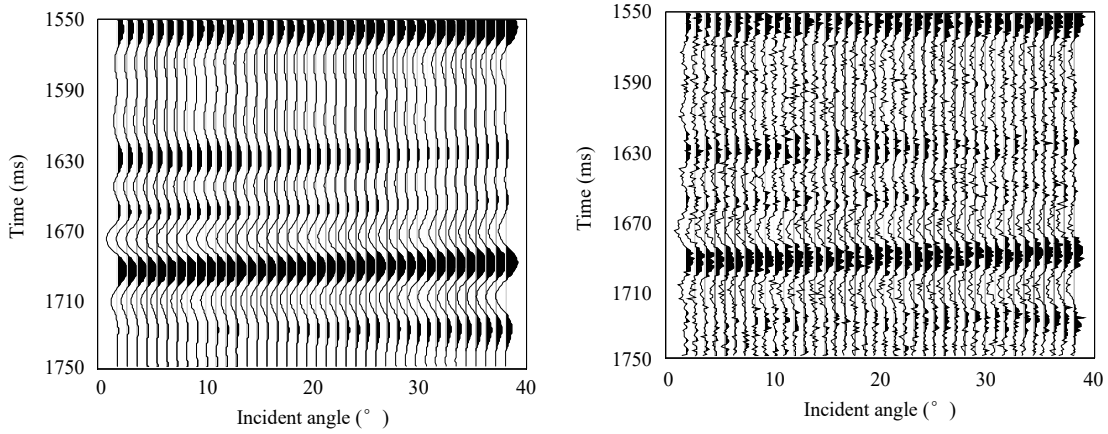

Figure 6. P-wave synthetic angle gathers: (**a**) without noise; (**b**) SNR = 2.

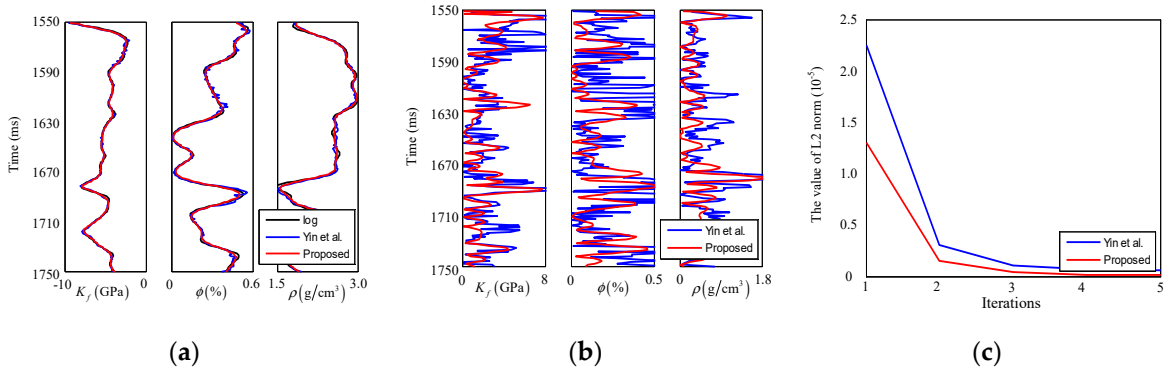

Figure 7. (**a**) Inversion results of the effective pore-fluid bulk modulus, porosity, and density by the linear and proposed methods; (**b**) Error; (**c**) The values of the L2 norm.

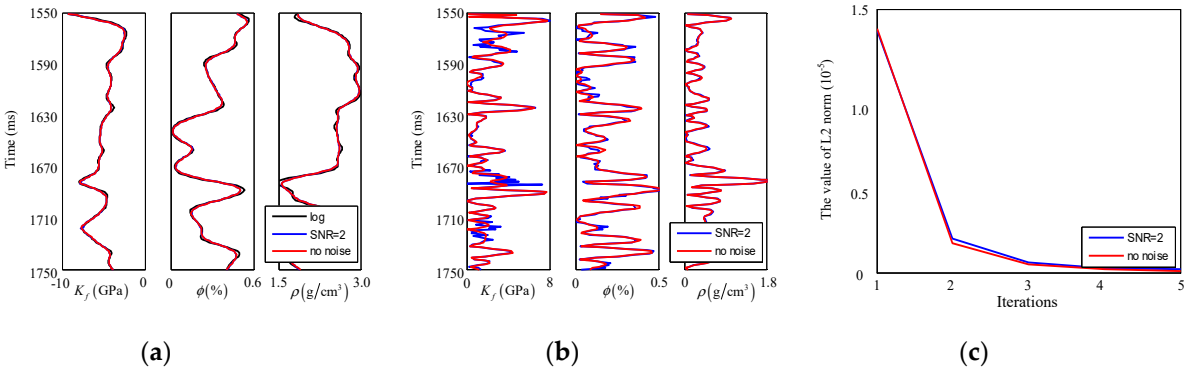

Figure 8. (**a**) Inversion results of the effective pore-fluid bulk modulus, porosity, and density based on the synthetic gathers with and without noise; (**b**) Error; (**c**) The values of the L2 norm.

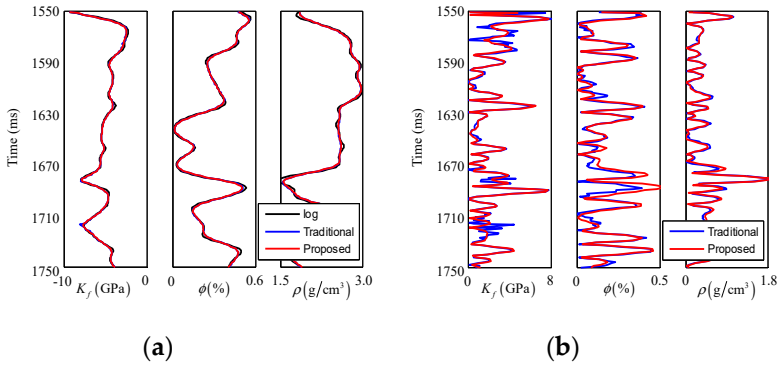

Figure 9. (**a**) Inversion results of the effective pore-fluid bulk modulus, porosity, and density by the fully nonlinear and proposed methods; (**b**) Error.

3.2. *Field Data Test*

Additionally, a real 2D dataset was used to measure the feasibility of the proposed method, with mainly sandstone reservoirs as the target layers. Figure 10 is the post-stack seismic section, with gas layers at 1.601 and 1.662 s, and water layers at 1.579, 1.620, 1.628, and 1.642 s, according to the logging interpretation. Based on the logging data, we calculated the effective pore-fluid bulk modulus to test its sensitivity to pore-fluid. The cross-plot of the pore-fluid bulk modulus and porosity is shown in Figure 11. The different pore-fluid types can be clearly identified by the pore-fluid bulk modulus. We transformed the pre-stack gathers from the offset domain to the angle domain and extracted angle gathers from 3° to 38°. A wavelet was statistically determined from the field seismic data for inversion. Finally, the proposed inversion method was applied to obtain the elastic parameters.

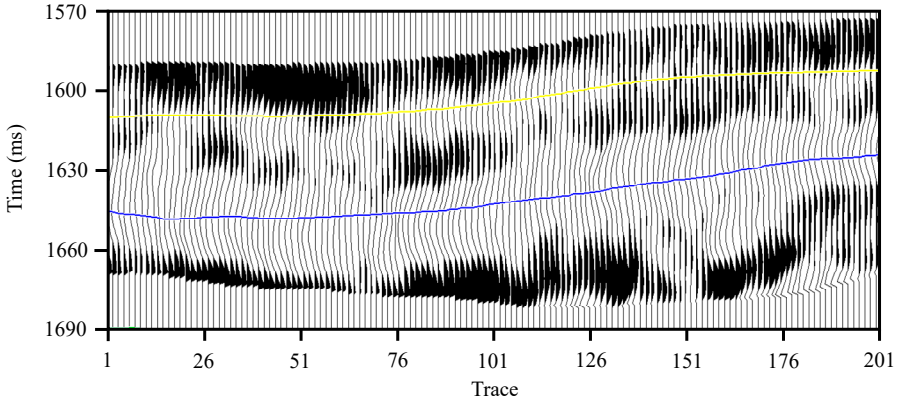

Figure 10. Field data seismic section.

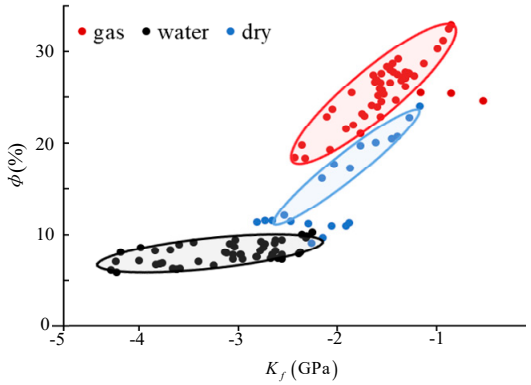

Figure 11. Cross-plot of the effective pore-fluid bulk modulus and porosity.

The inverted effective pore-fluid bulk modulus and density are displayed in Figure 12. In Figure 12a, the values of purple area range from −1.5 to −0.5 GPa, which means gas sand, while the red color ranges from −4 to −3 GPa, representing water sand. There are two purple areas matching the gas sandstone reservoirs in the profile of the effective pore-fluid bulk modulus. Four red layers exist and all correspond to the positions of water sandstone reservoirs. As shown in Figure 12b, the gas sand in purple has an approximate value of 2.30 g/cm^3. The value of the water sand in blue is around 2.38 g/cm^3. For the density profile, there are two purple layers and one blue layer. However, the first purple layer at 1.579 s is not gas sand but water sand. The bottom three layers cannot be identified on the profile. Note that the effective pore-fluid bulk modulus showed a better correlation with fluid interpretation than density did.

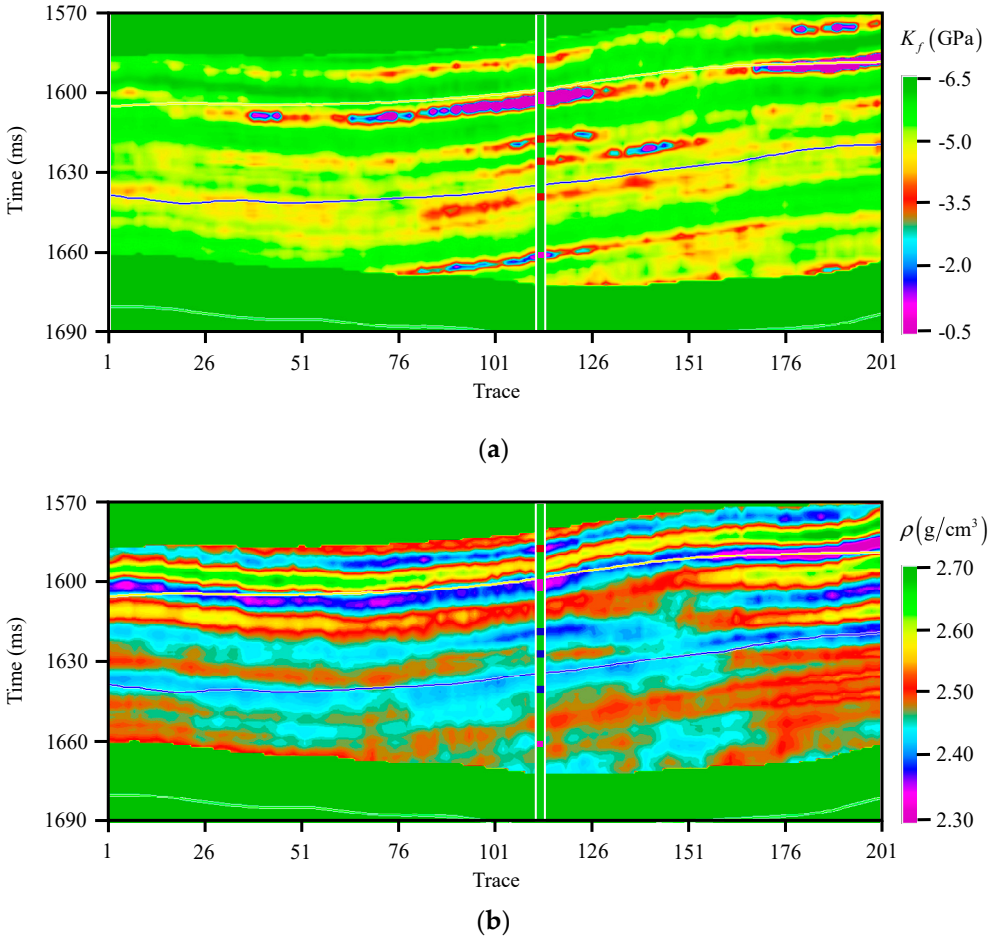

Figure 12. Inverted parameters sections: (**a**) the effective pore-fluid bulk modulus section; (**b**) the density section. Purple, black, and green indicate gas sand, water sand, and the surrounding rocks, respectively.

4. Discussion

In this study, we addressed three topics. First, we favored the effective pore-fluid bulk modulus as a fluid indicator to identify pore-fluid in a sandstone reservoir. A data analysis model followed and verifies the high sensitivity to pore-fluid change by the effective pore-fluid bulk modulus (Table 2 and Figure 1). With this in mind, a new high-order AVO approximation was deduced based on the Zoeppritz equations and Biot–Gassmann theory. Appendix A includes the detailed formula derivations. Figures 2–4 show the high accuracy and stability of this new approximation. Second, we introduce the series reversion and Bayesian theory to build a nonlinear AVO inversion method. The results of logging data tests showed that the proposed nonlinear inversion method had higher accuracy than the linear method (Figure 7). The stability and noise-insensitivity of the proposed method were high because of the Bayesian framework (Figure 8). The proposed method showed high accuracy and efficiency by comparison with the traditional fully nonlinear inversion method (Figure 9). The field data test showed the practicability of the proposed method and the strong identification ability of the effective pore-fluid bulk modulus (Figure 11). Third, we briefly illustrated the limitation and expectations of this work. Compared with other fluid indicators, the effective pore-fluid bulk modulus was more sensitive to pore-fluid change. However, this methodology was only applicable for sandstone reservoirs. Moreover, fluid indicators should be selected according to the actual reservoir conditions. An assumption that the lithology of the target reservoir was constant was made during the derivation of the new approximation. This presumption is inconsistent with real conditions, and will produce errors when applying the new approximation into field data. A new study direction would be to address this assumption. Finally, we use an AVO inversion method to obtain the effective pore-fluid

bulk modulus from seismic data. This method relies heavily on the initial model, which is difficult to build satisfactorily for field data inversion. Deep learning would be a promising alternative for the future inverted method.

5. Conclusions

An effective pore-fluid bulk modulus is regarded as a fluid indicator that can identify pore-fluid in sandstone. Based on the Zoeppritz equations and Biot–Gassmann theory, we first derived a high-order approximation that estimated the effective pore-fluid bulk modulus directly. By introducing the series reversion and Bayesian theory, a nonlinear AVO inversion method was proposed to invert the effective pore-fluid bulk modulus. Model results demonstrate that the high-order AVO approximation had higher precision than linear approximations and could be applied to AVO inversion. The results of the field data test show the stability, effectiveness, and feasibility of our method in identifying pore-fluid in a sandstone reservoir.

Author Contributions: Conceptualization, L.S., Y.S., D.C., and Y.L.; Data curation, L.S., D.C., and Y.S.; Funding acquisition, L.S., Y.L., and J.L.; Investigation, L.S. and Y.L.; Methodology, Y.S., D.C., and Y.L.; Resources, L.S. and Y.L.; Supervision, J.L.; Writing—original draft, L.S. and Y.S.; Writing—review & editing, Y.L. All authors have read and agreed to the published version of the manuscript.

Funding: This research was funded by the Important National Science & Technology Specific Project of China under contract 2016ZX05002005-003.

Conflicts of Interest: The authors declare no conflict of interest.

Appendix A

The contents of this appendix show the weighting coefficients before $\Delta K_f/\overline{K}_f$, $\Delta\phi/\overline{\phi}$, and $\Delta\rho/\overline{\rho}$ of $R_{PP}^{(1)}$, $R_{PP}^{(2)}$ and $R_{PP}^{(3)}$.

Appendix A.1. The Weighting Coefficients before $\Delta K_f/\overline{K}_f$, $\Delta\phi/\overline{\phi}$, and $\Delta\rho/\overline{\rho}$ of $R_{PP}^{(1)}$

$$R_{pp}^{(1)} = W_{11}\frac{\Delta K_f}{\overline{K}_f} + W_{12}\frac{\Delta\phi}{\overline{\phi}} + W_{13}\Delta\frac{\Delta\rho}{\overline{\rho}}\,, \tag{A1}$$

where

$$W_{11} = \frac{1}{4}\left(1 - \frac{\gamma_{dry}^2}{\gamma_{sat}^2}\right)\sec^2(\theta),$$

$$W_{12} = \frac{1}{4}\left(1 - \frac{\gamma_{dry}^2}{\gamma_{sat}^2}\right)\sec^2(\theta) + \left[\frac{1}{4}\frac{\gamma_{dry}^2}{\gamma_{sat}^2}\sec^2(\theta) - \frac{2}{\gamma_{sat}^2}\sin^2(\theta)\right]\gamma_\phi,$$

$$W_{13} = \frac{1}{2} - \frac{1}{4}\sec^2(\theta).$$

Appendix A.2. The Weighting Coefficients before $\Delta K_f/\overline{K}_f$, $\Delta\phi/\overline{\phi}$, and $\Delta\rho/\overline{\rho}$ of $R_{PP}^{(2)}$

$$R_{pp}^{(2)} = W_{21}\left(\frac{\Delta K_f}{\overline{K}_f}\right)^2 + W_{22}\frac{\Delta\phi^2}{\overline{\phi}} + W_{23}\frac{\Delta\rho^2}{\overline{\rho}} + W_{24}\frac{\Delta K_f}{\overline{K}_f}\frac{\Delta\phi}{\overline{\phi}} + W_{25}\frac{\Delta K_f}{\overline{K}_f}\frac{\Delta\rho}{\overline{\rho}} + W_{26}\frac{\Delta\phi}{\overline{\phi}}\frac{\Delta\rho}{\overline{\rho}}, \tag{A2}$$

where

$$W_{21} = \frac{1}{8}\left(1 - \frac{\gamma_{dry}^2}{\gamma_{sat}^2}\right)\left[\sin^2(\theta) + \frac{\gamma_{dry}^2}{\gamma_{sat}^2}\right],$$

$$W_{22} = \frac{1}{8}\left(1-\frac{\gamma_{dry}^2}{\gamma_{sat}^2}\right)\left[\sin^2(\theta)+\frac{\gamma_{dry}^2}{\gamma_{sat}^2}\right]+\left\{\begin{array}{c}\frac{1}{8}\frac{\gamma_{dry}^2}{\gamma_{sat}^2}\left[\sec^2(\theta)-\frac{\gamma_{dry}^2}{\gamma_{sat}^2}\right]\\ -\frac{1}{\gamma_{sat}^2}\left(1-\frac{1}{\gamma_{sat}}\right)\sin^2(\theta)\end{array}\right\}\gamma_\phi^2-\frac{1}{4}\frac{\gamma_{dry}^2}{\gamma_{sat}^2}\left(1-\frac{\gamma_{dry}^2}{\gamma_{sat}^2}\right)\gamma_\phi,$$

$$W_{23} = \frac{1}{8}\left(1-\frac{2}{\gamma_{sat}}\right)\sin^2(\theta),$$

$$W_{24} = \frac{1}{4}\left(1-\frac{\gamma_{dry}^2}{\gamma_{sat}^2}\right)\left[\sin^2(\theta)+\frac{\gamma_{dry}^2}{\gamma_{sat}^2}\right]-\frac{1}{4}\frac{\gamma_{dry}^2}{\gamma_{sat}^2}\left(1-\frac{\gamma_{dry}^2}{\gamma_{sat}^2}\right)\gamma_\phi,$$

$$W_{25} = -\frac{1}{4}\left(1-\frac{\gamma_{dry}^2}{\gamma_{sat}^2}\right)\sin^2(\theta),$$

$$W_{26} = -\frac{1}{4}\left(1-\frac{\gamma_{dry}^2}{\gamma_{sat}^2}\right)\sin^2(\theta)+\frac{1}{\gamma_{sat}^2}\left(1-\frac{\gamma_{dry}^2}{4}\right)\sin^2(\theta)\gamma_\phi.$$

Appendix A.3. The Weighting Coefficients before $\Delta K_f/\overline{K}_f$, $\Delta\phi/\overline{\phi}$, and $\Delta\rho/\overline{\rho}$ of $R_{PP}^{(3)}$

$$\begin{aligned}R_{pp}^{(3)} = {} & W_{30}\frac{\Delta K_f{}^3}{\overline{K}_f}+W_{31}\frac{\Delta\phi^3}{\overline{\phi}}+W_{32}\frac{\Delta\rho^3}{\overline{\rho}}+W_{33}\frac{\Delta K_f{}^2}{\overline{K}_f}\frac{\Delta\phi}{\overline{\phi}}+W_{34}\frac{\Delta K_f{}^2}{\overline{K}_f}\frac{\Delta\rho}{\overline{\rho}}+W_{35}\frac{\Delta\phi^2}{\overline{\phi}}\frac{\Delta K_f}{\overline{K}_f}+W_{36}\frac{\Delta\phi^2}{\overline{\phi}}\frac{\Delta\rho}{\overline{\rho}}\\ & +W_{37}\frac{\Delta\rho^2}{\overline{\rho}}\frac{\Delta K_f}{\overline{K}_f}+W_{38}\frac{\Delta\rho^2}{\overline{\rho}}\frac{\Delta\phi}{\overline{\phi}}+W_{39}\frac{\Delta K_f}{\overline{K}_f}\frac{\Delta\phi}{\overline{\phi}}\frac{\Delta\rho}{\overline{\rho}},\end{aligned} \tag{A3}$$

where

$$W_{30} = \frac{3}{64}\left(1-\frac{\gamma_{dry}^4}{\gamma_{sat}^4}\right)\sin^2(\theta)-\frac{3}{64}\frac{\gamma_{dry}^2}{\gamma_{sat}^2}\left(1+\frac{1}{3}\sin^2(\theta)\right)+\frac{1}{64}+\frac{7}{64}\frac{\gamma_{dry}^4}{\gamma_{sat}^4}-\frac{5}{64}\frac{\gamma_{dry}^6}{\gamma_{sat}^6}\left(1-\frac{1}{5}\sin^2(\theta)\right),$$

$$\begin{aligned}W_{31} = {} & \left[\tfrac{3}{64}\left(1-\tfrac{\gamma_{dry}^4}{\gamma_{sat}^4}\right)\sin^2(\theta)-\tfrac{3}{64}\tfrac{\gamma_{dry}^2}{\gamma_{sat}^2}\left(1+\tfrac{1}{3}\sin^2(\theta)\right)\tfrac{1}{64}+\tfrac{7}{64}\tfrac{\gamma_{dry}^4}{\gamma_{sat}^4}-\tfrac{5}{64}\tfrac{\gamma_{dry}^6}{\gamma_{sat}^6}\left(1-\tfrac{1}{5}\sin^2(\theta)\right)\right]\\ & +\left[\begin{array}{l}\frac{5}{64}\frac{\gamma_{dry}^6}{\gamma_{sat}^6}\left(1-\frac{1}{5}\sin^2(\theta)\right)-\frac{1}{2}\frac{1}{\gamma_{sat}^2}\left(1+\frac{\gamma_{dry}^2}{\gamma_{sat}^2}\right)\sin^2(\theta)+\frac{1}{16}\frac{\gamma_{dry}^2}{\gamma_{sat}^2}\sec^2(\theta)-\frac{1}{8}\frac{\gamma_{dry}^4}{\gamma_{sat}^4}\left(1-\frac{1}{\gamma_{sat}^2}\sin^2(\theta)\right)\\ +\frac{3}{4}\frac{1}{\gamma_{sat}^3}\sin^2(\theta)\end{array}\right]\gamma_\phi^3\\ & +\left[\begin{array}{l}\frac{1}{8}\frac{1}{\gamma_{sat}^2}\sin^2(\theta)-\frac{3}{64}\frac{\gamma_{dry}^2}{\gamma_{sat}^2}\left(1+\frac{\gamma_{dry}^4}{\gamma_{sat}^4}\right)\sin^2(\theta)-\frac{1}{4}\frac{\gamma_{dry}^2}{\gamma_{sat}^2}\left(1-\frac{1}{2}\frac{\gamma_{dry}^2}{\gamma_{sat}^2}\right)\sin^2(\theta)\\ -\frac{11}{32}\frac{\gamma_{dry}^4}{\gamma_{sat}^4}\left(1-\frac{3}{11}\sin^2(\theta)\right)+\frac{7}{64}\frac{\gamma_{dry}^2}{\gamma_{sat}^2}\left(1+\frac{15}{7}\frac{\gamma_{dry}^4}{\gamma_{sat}^4}\right)\end{array}\right]\gamma\\ & +\left[\left(\tfrac{1}{4}\tfrac{\gamma_{dry}^2}{\gamma_{sat}^2}-\tfrac{1}{2}\tfrac{1}{\gamma_{sat}^3}\right)\left(1-\tfrac{\gamma_{dry}^2}{\gamma_{sat}^2}\right)\sin^2(\theta)-\tfrac{15}{64}\tfrac{\gamma_{dry}^6}{\gamma_{sat}^6}\left(1-\tfrac{1}{5}\sin^2(\theta)\right)+\tfrac{23}{64}\tfrac{\gamma_{dry}^4}{\gamma_{sat}^4}\left(1-\tfrac{3}{23}\sin^2(\theta)\right)-\tfrac{1}{8}\tfrac{\gamma_{dry}^2}{\gamma_{sat}^2}\right]\gamma_\phi^2\end{aligned},$$

$$W_{32} = \frac{1}{64}-\frac{3}{64}\sin^2(\theta)+\frac{1}{16}\frac{1}{\gamma_{sat}}\sin^2(\theta),$$

$$\begin{aligned}W_{33} = {} & \left[\tfrac{9}{64}\left(1-\tfrac{\gamma_{dry}^4}{\gamma_{sat}^4}\right)\sin^2(\theta)-\tfrac{9}{64}\tfrac{\gamma_{dry}^2}{\gamma_{sat}^2}\left(1+\tfrac{1}{3}\sin^2(\theta)\right)+\tfrac{3}{64}+\tfrac{21}{64}\tfrac{\gamma_{dry}^4}{\gamma_{sat}^4}-\tfrac{15}{64}\tfrac{\gamma_{dry}^6}{\gamma_{sat}^6}\left(1-\tfrac{1}{5}\sin^2(\theta)\right)\right]\\ & +\left[\begin{array}{l}\frac{1}{8}\frac{1}{\gamma_{sat}^2}\sin^2(\theta)-\frac{3}{64}\frac{\gamma_{dry}^2}{\gamma_{sat}^2}\left(1+\frac{\gamma_{dry}^4}{\gamma_{sat}^4}\right)\sin^2(\theta)-\frac{1}{4}\frac{\gamma_{dry}^2}{\gamma_{sat}^2}\left(1-\frac{1}{2}\frac{\gamma_{dry}^2}{\gamma_{sat}^2}\right)\sin^2(\theta)-\frac{11}{32}\frac{\gamma_{dry}^4}{\gamma_{sat}^4}\left(1-\frac{3}{11}\sin^2(\theta)\right)\\ +\frac{7}{64}\frac{\gamma_{dry}^2}{\gamma_{sat}^2}\left(1+\frac{15}{7}\frac{\gamma_{dry}^4}{\gamma_{sat}^4}\right)\end{array}\right]\gamma_\phi\end{aligned},$$

$$W_{34} = \frac{1}{32}\frac{\gamma_{dry}^2}{\gamma_{sat}^2}\left(1+5\sin^2(\theta)\right)-\frac{1}{64}\frac{\gamma_{dry}^4}{\gamma_{sat}^4}\sec^2(\theta)-\frac{1}{64}-\frac{9}{64}\sin^2(\theta),$$

$$W_{35} = \left[\frac{9}{64}\left(1-\frac{\gamma_{dry}^4}{\gamma_{sat}^4}\right)\sin^2(\theta) - \frac{9}{64}\frac{\gamma_{dry}^2}{\gamma_{sat}^2}\left(1+\frac{1}{3}\sin^2(\theta)\right) + \frac{3}{64} + \frac{21}{64}\frac{\gamma_{dry}^4}{\gamma_{sat}^4} - \frac{15}{64}\frac{\gamma_{dry}^6}{\gamma_{sat}^6}\left(1-\frac{1}{5}\sin^2(\theta)\right)\right]$$
$$+2\left[\begin{array}{l}\frac{1}{8}\frac{1}{\gamma_{sat}^2}\sin^2(\theta) - \frac{3}{64}\frac{\gamma_{dry}^2}{\gamma_{sat}^2}\left(1+\frac{\gamma_{dry}^4}{\gamma_{sat}^4}\right)\sin^2(\theta) - \frac{1}{4}\frac{\gamma_{dry}^2}{\gamma_{sat}^2}\left(1-\frac{1}{2}\frac{\gamma_{dry}^2}{\gamma_{sat}^2}\right)\sin^2(\theta) - \frac{11}{32}\frac{\gamma_{dry}^4}{\gamma_{sat}^4}\left(1-\frac{3}{11}\sin^2(\theta)\right)\\ +\frac{7}{64}\frac{\gamma_{dry}^2}{\gamma_{sat}^2}\left(1+\frac{15}{7}\frac{\gamma_{dry}^4}{\gamma_{sat}^4}\right)\end{array}\right]\gamma_\phi\ ,$$
$$+\left[\left(\frac{1}{4}\frac{\gamma_{dry}^2}{\gamma_{sat}^2} - \frac{1}{2}\frac{1}{\gamma_{sat}^3}\right)\left(1-\frac{\gamma_{dry}^2}{\gamma_{sat}^2}\right)\sin^2(\theta) - \frac{15}{64}\frac{\gamma_{dry}^6}{\gamma_{sat}^6}\left(1-\frac{1}{5}\sin^2(\theta)\right) + \frac{23}{64}\frac{\gamma_{dry}^4}{\gamma_{sat}^4}\left(1-\frac{3}{23}\sin^2(\theta)\right) - \frac{1}{8}\frac{\gamma_{dry}^2}{\gamma_{sat}^2}\right]\gamma_\phi^2$$

$$W_{36} = \frac{1}{32}\frac{\gamma_{dry}^2}{\gamma_{sat}^2}\left(1+5\sin^2(\theta)\right) - \frac{1}{64}\frac{\gamma_{dry}^4}{\gamma_{sat}^4}\sec^2(\theta) - \frac{1}{64} - \frac{9}{64}\sin^2(\theta) + \left[\begin{array}{l}\frac{3}{4}\frac{1}{\gamma_{sat}^2}\left(1-\frac{1}{\gamma_{sat}}\right)\sin^2(\theta)\\ -\frac{1}{8}\frac{\gamma_{dry}^2}{\gamma_{sat}^2}\left(1-\frac{2}{\gamma_{sat}^2}\right)\sin^2(\theta)\\ -\frac{1}{64}\frac{\gamma_{dry}^4}{\gamma_{sat}^4}\sec^2(\theta)\end{array}\right]\gamma_\phi^2\ ,$$
$$+\left(1-\frac{\gamma_{dry}^2}{\gamma_{sat}^2}\right)\left(\frac{1}{4}\frac{1}{\gamma_{sat}^2}\sin^2(\theta) - \frac{1}{32}\frac{\gamma_{dry}^2}{\gamma_{sat}^2}\sec^2(\theta)\right)\gamma_\phi$$

$$W_{37} = \left(1-\frac{\gamma_{dry}^2}{\gamma_{sat}^2}\right)\left(\frac{9}{64}\sin^2(\theta) - \frac{1}{8}\frac{1}{\gamma_{sat}}\sin^2(\theta) - \frac{1}{64}\right),$$

$$W_{38} = \left(1-\frac{\gamma_{dry}^2}{\gamma_{sat}^2}\right)\left(\frac{9}{64}\sin^2(\theta) - \frac{1}{8}\frac{1}{\gamma_{sat}}\sin^2(\theta) - \frac{1}{64}\right) + \left[\begin{array}{l}-\frac{1}{64}\frac{\gamma_{dry}^2}{\gamma_{sat}^2}\left(1-9\sin^2(\theta)\right) - \frac{1}{16}\frac{1}{\gamma_{sat}}\left(1+2\frac{\gamma_{dry}^2}{\gamma_{sat}^2}\right)\sin^2(\theta)\\ -\frac{1}{8}\frac{1}{\gamma_{sat}^2}\sin^2(\theta)\end{array}\right]\gamma_\phi,$$

$$W_{39} = \frac{1}{16}\frac{\gamma_{dry}^2}{\gamma_{sat}^2}\left(1+5\sin^2(\theta)\right) - \frac{1}{32}\frac{\gamma_{dry}^4}{\gamma_{sat}^2}\sec^2(\theta) - \frac{1}{32} - \frac{9}{32}\sin^2(\theta) + \left(1-\frac{\gamma_{dry}^2}{\gamma_{sat}^2}\right)\left[\begin{array}{l}\frac{1}{4}\frac{1}{\gamma_{sat}^2}\sin^2(\theta)\\ -\frac{1}{32}\frac{\gamma_{dry}^2}{\gamma_{sat}^2}\sec^2(\theta)\end{array}\right]\gamma_\phi.$$

References

1. Smith, G.C.; Gidlow, P.M. Weighting stacking for rock property estimation and detection of gas. *Geophys. Prospect.* **1987**, *35*, 993–1014. [CrossRef]
2. Fatti, J.L.; Smith, G.C.; Vail, P.J.; Strauss, P.J.; Levitt, P.R. Detection of gas in sandstone reservoirs using AVO analysis: A 3-D seismic case history using the Geostack technique. *Geophysics* **1994**, *59*, 1362–1376. [CrossRef]
3. Goodway, B.; Chen, T.; Downton, J. *Improved AVO Fluid Detection and Lithology Discrimination Using Lame Petrophysical Parameters: "λρ", "μρ" and "λ/μ Fluid Stack" from P and S Inversions*; SEG Expanded Abstracts: Dallas, TX, USA, 1997; pp. 183–186.
4. Quakenbush, M.; Shang, B.; Tuttle, C. Poisson impedance. *Lead. Edge* **2006**, *25*, 128–138. [CrossRef]
5. Russell, B.H.; Gray, D.; Hampson, D.P. Linearized AVO and poroelasticity. *Geophysics* **2011**, *76*, C19–C29. [CrossRef]
6. Zhang, S.; Yin, X.; Zhang, F. *Quasi Fluid Modulus for Delicate Lithology and Fluid Discrimination*; SEG Expanded Abstracts: Denver, CO, USA, 2010; pp. 404–408.
7. Yin, X.; Zhang, S. Bayesian inversion for effective pore-fluid bulk modulus based on fluid-matrix decoupled amplitude variation with offset approximation. *Geophysics* **2014**, *79*, R221–R232. [CrossRef]
8. Yin, X.; Wang, H.; Cao, D.; Zhou, Q.; Sun, W. Three-term AVO approximation of K_f-f_m-ρ and prestack seismic inversion for deep reservoirs. *Oil Geophys. Prospect.* **2018**, *53*, 129–135.
9. Hilterman, F.J. *Seismic Amplitude Interpretation*; Society of Exploration Geophysicists: Tulsa, OK, USA, 2001; Volume 4.
10. Zoeppritz, K. Erdbebenwellen VIII B: Über die Reflexion and Durchgang seismischer Wellen durch Unstetigkeitsflächen. *Gott. Nachr.* **1919**, *1*, 66–84.
11. Keys, R.G. Polarity reversals in reflections from layered media. *Geophysics* **1989**, *54*, 900–905. [CrossRef]
12. Kim, S.; Innanen, K. Linear and nonlinear poroelastic AVO. *CREWES Res. Rep.* **2013**, *25*, 1–28.
13. Han, D.; Batzle, M. *Gain Function and Hydrocarbon Indicators*; SEG Expanded Abstracts: Dallas, TX, USA, 2003; pp. 1695–1698.

14. Nur, A.; Mavko, G.; Dvorkin, J.; Galmudi, D. Critical porosity: A key to relating physical properties to porosity in rocks. *Lead. Edge* **1998**, *17*, 357–362. [CrossRef]
15. Aki, K.; Richards, P.G. *Quantitative Seismology*; W. H. Freeman and Company: San Francisco, CA, USA, 1980.
16. De Nicolao, A.; Drufuca, G.; Rocca, F. Eigenvalues and eigenvectors of linearized elastic inversion. *Geophysics* **1993**, *58*, 670–679. [CrossRef]
17. Russell, B.H.; Hedlin, K.; Hilterman, F.J. Fluid-property discrimination with AVO: A Biot-Gassmann perspective. *Geophysics* **2003**, *68*, 29–39. [CrossRef]
18. Russell, B.H.; Gray, D.; Hampson, D.P.; Lines, L.R. Linearized AVO and poroelasticity. *CREWES Res. Rep.* **2006**, *18*, 1–25. [CrossRef]
19. Frank, H.W.; Tat, S.Y. New applications of non-linear chirp scaling in SAR data processing. *IEEE Trans. Geosci. Remote Sens.* **2001**, *39*, 946–953.
20. Zhang, H.; Weglein, A.B. Direct nonlinear inversion of multiparameter 1D elastic media using the inverse scattering series. *Geophysics* **2009**, *74*, WCD15–WCD27. [CrossRef]
21. Zhou, L.; Li, J.Y.; Chen, X.H. Nonlinear three-term AVO inversion based on exact Zoeppritz equation. *Chin. J. Geophys.* **2016**, *59*, 2663–2673.